This manuscript is a pre-print and has been accepted for publication in Tectonophysics. After proof reading, the final version of the manuscript will be available via the "Peer-reviewed Publication DOI" on right hand side of this webpage. Please feel free to contact the corresponding authors directly. We welcome feedback.

Laponite gels - visco-elasto-plastic analogues for geological laboratory modelling

Uchitha N. Arachchige*, Alexander R. Cruden, Roberto Weinberg

School of Earth, Atmosphere and Environment, Monash University, 9 Rainforest Walk, Clayton, VIC 3800, Australia

* Corresponding author: uchitha.nissankaarachchige@monash.edu

Abstract

Laponite® is a synthetic clay that, depending on concentration, temperature and curing time, forms a clear, transparent thixotropic fluid or brittle visco-elasto-plastic gel when mixed with water. Here we present the results of rheological and mechanical testing of gel-forming Laponite RD (LRD) to evaluate its suitability as a rock analogue in laboratory analogue experiments. Rheological tests of 2 – 4 wt. % concentrations of LRD in deionised water were carried out at temperatures between 20 and 50 °C, and after curing times of 3 to 14 days. Our results show that LRD gels change from a brittle, elastic-dominant, linear viscoelastic material to a plastic material as shear strain increases. The linear viscoelastic region occurs at shear strains, $\gamma < 10$ % after which the material yields and then undergoes strain hardening before a peak stress occurs at $\gamma = 15 – 20$ %. LRD then strain softens up to $\gamma < 26.2$ %, beyond which it behaves as a plastic material. Empirical equations are provided that predict increases in the Young's and complex shear moduli of LRD with increasing concentration and ageing time. LRD can be used to model elastic deformation when $\gamma < 10$ % at a shear strain rate of 0.1 s^{-1} and plastic deformation when $\gamma > 26.2$%. LRD is an ideal material for modelling the behaviour of rocks during the emplacement of magma and the propagation of brittle fractures in the upper crust. Its ease of preparation, low surface tension, full transparency, chemical and biological stability and photoelastic properties provide further advantages for analogue laboratory modelling compared to other frequently used visco-elastic gels, such as pig skin gelatine.

Keywords: Laponite RD; analogue material; rheology; yield stress; visco-elasto-plastic; magma emplacement and crack propagation

1. Introduction

Geological processes such as the transport and emplacement of magma in dykes and sills in the Earth's crust and associated host rock deformation are important for the development of upper crustal magma plumbing systems and the formation of magmatic ore deposits (Barnes et al., 2016; Magee et al., 2016). Although field and geophysical methods are used to study these processes either remotely or in exhumed ancient examples (e.g., Magee et al., 2018), direct, detailed and quantitative analysis of dyke and sill emplacement is typically carried out through analogue and/or numerical modelling (Galland et al., 2009; Bunger and Cruden, 2011; Kavanagh et al., 2015; Schmiedel et al., 2019). The reproducibility of natural geological structures at laboratory time and length scales, and the controllability of all relevant parameters using model scaling theory are powerful aspects of the analogue modelling approach (Kavanagh et al., 2006, 2018). Properly scaled materials and setups in laboratory experiments can therefore provide a better understanding of natural processes, and results can be compared to field and geophysical observations, and numerical analyses (Kavanagh et al., 2018; Reber et al., 2020).

Visco-elasto-plastic Laponite gels (3.3 wt. %) with short curing times (up to 240 min) have been used as country rock analogues for two dimensional experiments of magma emplacement in a Hele-Shaw cell (Bertelsen et al., 2018). These authors noted that the material properties of Laponite gels are not yet sufficiently well characterised for use as natural rock analogues in geological laboratory experiments. Here we report results of a systematic rheological study of Laponite RD® (LRD) gels in order to evaluate their suitability as host rocks in analogue modelling of magma emplacement processes, and other experimental tectonic applications.

Laponite® has been studied extensively in the polymer and clay sciences, and aqueous solutions of Laponite synthetic clays have attracted considerable interest as a rheological modifier for various applications such as surface coatings, consumer care products, paints, emulsion stabilisers, and mineral and hydrocarbon extraction technologies. Aqueous dispersions of Laponite with different concentrations and ionic strengths have received much attention in the colloid and polymer sciences and their gel or glass-like behaviours (Bonn et al., 1999), surface chemistry, basic rheological properties (Morariu et al., 2009; Pek-Ing and Yee-Kwong, 2015), and colloidal phase behaviour (Cummins, 2007; Ruzicka and Zaccarelli, 2011; Mohanty and Joshi, 2016) are well characterised.

LRD has several advantages as an elastic host rock analogue for laboratory modelling of magma transport and pressurized crack propagation compared to commonly used semi-transparent pig skin gelatine (Kavanagh et al., 2013; Brizzi et al., 2016; van Otterloo and Cruden, 2016). LRD is a gel forming grade of Laponite that is fully transparent, regardless of concentration and sample age. LRD gels (Fig. 1) are chemically and biologically stable viscoelastic solids with photo-elastic properties (Ruzicka and Zaccarelli, 2011; Kaushal and Joshi, 2014; Galland et al., 2015; Kavanagh et al., 2018). They have lower surface tension with water (72.8 mJ/m^2, Norris et al., 1993) and glycerol (64 mJ/m^2, Norris et al., 1993) compared to pig skin gelatine (1 J/ m^2; Kavanagh et al., 2013), which minimizes surface tension effects in geological experiments. After initial preparation, LRD mixtures remain in a weak solution state after a few minutes of curing (0 – 60 min), while the gel state is reached after several hours (~ 120 min) (Kaushal and Joshi, 2014; Bertelsen et al., 2018a). The rheological properties reported here are for LRD gels that have been cured over 3 to 14 days.

2. General properties of Laponite RD

2.1. Composition and structure

Laponite RD® (LRD; manufactured by BYK Additives and Instruments) is a gel-forming grade of a synthetic sheet silicate with a crystal structure and chemical composition similar to the natural clay mineral hectorite (Nuemann, 1965; Cummins, 2007; Wallace and Rutherford, 2015). Disc-shaped, nearly uniform Laponite crystals ($Si_8Mg_{5.45}Li_{0.4}O_{24}Na_{0.7}$) comprise one octahedral coordinated magnesium or aluminium oxide layer sandwiched in between two layers of tetrahedral coordinated silica (Fig. 2a). The unit cell has an overall net negative charge of approximately 700 electron charges, which becomes neutralised when interlayer Na+ ions are absorbed on to the surface of the crystal (Bonn et al., 1999; Cummins, 2007; Lapasin et al., 2017). As reported by BYK Additives and Instruments (2014), the bulk density of LRD is 1000 kg/m^3 and a single Laponite crystal is disc shaped with a typical diameter of 25 nm and height of 0.92 nm (Fig. 2b).

2.2. Sample preparation

In order to achieve full hydration when LRD powder is mixed with water, our sample preparation followed the laboratory-scale mixing procedure recommended by the manufacturer. Room temperature (19 - 23°C), filtered, deionised water is first poured into a high-speed, 3L capacity commercial blender. Unlike gelatine, LRD can be mixed and forms a gel at room temperature without cooling, which is an added advantage. With the blender rotating, the desired amount of Laponite powder is gradually added to a known volume of deionised water

over a period between 10 to 30 s. The sample is then blended for up to 20 min to achieve full hydration and dispersion of the LRD-water mixture. The LRD mixtures are then poured into containers and left to form transparent gels. The containers were sealed to prevent evaporation of water. Air bubbles typically form in the mixture during high-speed stirring, but they eventually rise to the surface resulting a bubble-free gel sample. Samples with >4 wt. % LRD are impossible to use because they rapidly form a gel before complete mixing occurs. For concentrations <2 wt. % LRD, samples remain in the solution state for much longer times (a few weeks) before a gel structure forms. Therefore, for practical purposes, batches with concentrations of 2, 2.5, 3, 3.5 and 4 wt. % of LRD in deionised water were prepared for rheological measurements.

3. Methods

3.1 Theoretical background

Combined solid and fluid dynamic approaches are required for complete characterisation of viscoelastic materials that are commonly used in experimental tectonics (Ranalli 1995; ten Grotenhuis et al., 2002; Boutelier et al., 2007; Di Giuseppe et al., 2009). The first approach uses Hooke's law for materials that behave as elastic solids, in which stress (σ) is proportional to the strain (γ) and independent of the strain rate ($\dot{\gamma}$). Elastic solids tend to store energy rather than dissipate it before failing by yielding or brittle fracturing.

A fluid dynamic approach is used to characterise viscous fluids, which dissipate energy. Newtonian viscous materials show a linear proportionality between stress (σ) and strain rate ($\dot{\gamma}$), while in non-Newtonian viscous materials the relationship is non-linear (ten Grotenhuis et al., 2002). Material is considered either shear thickening or shear thinning in the non-Newtonian viscous regime if the viscosity increases or decreases, respectively, with increasing strain rate.

3.1.1. Viscoelastic deformation

Viscoelastic materials respond to stress by a combination of elastic and viscous deformation. When subjected to an applied stress, a viscoelastic material may display strain-independent linear viscoelastic and strain-dependent non-linear viscoelastic regimes. The linear and non-linear domains of a viscoelastic material are usually characterised by an elastic storage modulus (G'), representing elastic energy stored during deformation and a loss modulus (G''), representing energy lost by viscous dissipation during and after deformation (Di Giuseppe et al., 2009; Mezger 2006; Xue et al., 2017). For a material in the linear viscoelastic regime,

the resulting shear stress (τ) is out of phase with the applied shear strain according to the relationship (Ferry, 1980):

$$\tau = \gamma_0(G'\sin(\omega t) + G''\cos(\omega t)) \quad (1)$$

Where ω is the frequency and γ_0 is the maximum amplitude of the shear strain. G′ and G″ are the frequency dependent elastic storage and viscous loss moduli, respectively.

The complex shear modulus is derived from the storage and loss moduli:

$$G^* = G' + iG'' \quad (2)$$

where the storage modulus is the real part and the loss modulus is the imaginary part and the moduli are perpendicular vectors (Mezger 2006; van Otterloo and Cruden, 2016). The complex shear modulus can be obtained from (Mezger 2006):

$$G^* = \sqrt{G'^2 + G''^2} \quad (3)$$

A typical rheological characterisation of a viscoelastic material is illustrated in Fig. 3a. This material shows viscous dominant viscoelastic behaviour in the lower frequency range where G″ > G′

On the other hand, in the higher frequency regions where G′ reaches a plateau value and where the G′/G″ ratio is high (G′ >> G″), the material shows elastic dominant viscoelastic behaviour, which can be described by Hooke's Law. In the cross over region where the elastic and loss moduli have similar values (G′~G″), the material is viscoelastic. The point at which G′ and G″ cross over determines the frequency (ω_c) that gives the Maxwell relaxation time ($t_m = 1/\omega_c$) of the material.

The complex Young's modulus (E*) relates to the complex shear modulus according to (Timoshenko and Goodier, 1970; van Krevelen, 1990):

$$E^* = 2G^*(1+\nu) \quad (4)$$

where, ν is Poisson's ratio, which describes the compressibility of the material.

3.1.2. Plastic deformation

When the elastic limit is reached in most materials, strain is no longer proportional to the applied stress and atomic bonds start to break. When this occurs, the material can no longer return to its original structure and the deformation is permanent, known as plastic behaviour (Per et al., 1983; Irgens, 2008). The stress under which noticeable plastic deformation occurs is called the yield stress, τ_y. As the material deforms at stresses > τ_y, the corresponding strain is not recoverable (Fig. 3b).

3.1.3. Brittle elastic deformation

For complete characterisation of a material's properties it is also important to understand its behaviour at large strains and failure. At large strain, a material can fail by either forming brittle-elastic fractures or by permanent plastic flow. Brittle fractures are considered to originate in the elastic region at a critical stress (brittle strength), when all bonds between structural elements in a macroscopic plane within the material break. This results in failure of the structure of the material at larger scale and a sudden drop in stress (Di Giuseppe et al., 2009).

3.1.4. Rheological models

Common rheological models (Fig. 4) used to explain viscoelastic behaviours comprise a linear elastic component represented by a spring and a Newtonian viscous component represented by a dashpot. They can either be in series (Maxwell model; Fig. 4d) or in parallel (Kelvin-Voigt model; Fig. 4c) (Barnes et al.,1989; Chhabra, 2010). The viscosity to modulus of rigidity ratio (η/G) defines the Maxwell relaxation time (t_m) (Bailey, 2006; Chhabra, 2010) in the Maxwell model, and the retardation time (t_{kv}) in the Kelvin-Voigt model. After the application of a load, a Maxwell element will accumulate permanent viscous deformation over time, whereas a Kelvin-Voigt material will return to its undeformed state. However, both the Maxwell and Kelvin-Voigt models can be used to represent either the short-term, long-term or transient creep behaviour of a material, but not all of them together. To overcome this shortcoming, a Burgers model, which has Maxwell and Kelvin-Voigt elements in series, is commonly used to account for the steady-state creep behaviour of many materials (Fig. 4h).

Perfectly plastic behaviour is modelled using a frictional element with a yield stress below which no strain occurs, analogous to a rigid block sliding on a rough surface (Fig. 4e). Rheological models for elastic-plastic behaviour (Fig. 4f) are made up of a spring and frictional element in series (Barnes et al., 1989; Irgens, 2008). This model behaves ideally elastic for stresses below the yield stress, τ_y, and perfectly plastic at stresses above τ_y. Visco-plastic rheological models (Fig. 4g) have a dashpot in parallel with a frictional element, also known as a Bingham plastic. When the applied stress in such a material is $< \tau_y$, no deformation is possible; at higher stresses the material flows linearly.

3.2 Rheological testing methods

Samples of LRD were subjected to a series of rheological tests performed using an Anton Paar Physica MCR 301 rheometer. A flat parallel-plate geometry (Fig. 5) with 1 mm gap was used, and the instrument and measurement accuracy are < 0.1 % and 5 %, respectively (Di Giuseppe et al., 2009). After the desired curing time, a carefully sliced sample was placed on the bottom plate of the rheometer and the top plate was lowered slowly onto it. To minimise

possible alterations of the structure of the sample during loading the sample was left for about 30 minutes between the parallel plates before starting the measurements. To control the effects of temperature and evaporation on the sample, the parallel plate measuring system was coupled with a closed Peltier hood during measurements. Both oscillation (a.k.a. dynamic) and rotational testing methods were used to impose shear stresses, shear strains and shear strain rates on the samples and to measure dynamic moduli and shear strength of the material, respectively. All tests were performed under constant zero normal stress from the upper plate. The shear strain, shear stress and shear strain rate are controlled by changing the angular displacement (amplitude), torque and angular velocity of the upper plate of the rheometer, respectively. Shear strain rate in oscillation tests is also controlled by varying the oscillation frequency, ω. In order to evaluate the reproducibility of the measurements and assess for possible rheometer plate slip effects, three separate tests were conducted on each LRD concentration, and signs of any detachment of the sample from the parallel plates were carefully assessed after each measurement. Moreover, we carefully compared our amplitude sweep and frequency sweep test results with those of Mourchid et al. (1998) and Morariu and Bercea (2011). We consistently found that the results for the three repeated tests for each sample were reproducible and very similar to previous studies, indicating that rheometer plate slippage is unlikely to have occurred. The following section provides a brief outline of each test method and its significance.

3.2.1 Oscillatory tests

Oscillatory amplitude sweep tests were used to determine the linear viscoelastic range of LRD in its gel state. In these tests, the shear strain applied to samples of different concentration was varied from 0.01 to 100 % while the oscillation frequency and temperature were kept constant (ω = 0.1 s^{-1}, T = 22.5 °C; curing time = 3 days; See Table 1 for details of measurements). The linear viscoelastic range (Fig. 6) is defined as the region where the dynamic moduli have constant values over a range of imposed shear strain values below a shear strain threshold (γ_c). When γ_c is exceeded, the dynamic moduli either increase (G″; viscous component) or decrease (G′; elastic component) and the material behaviour becomes strain-dependent or non-linear. Furthermore, Brizzi et al. (2016) have shown that in amplitude sweep tests, constant plateau values of G′ and G″ reflect an equilibrium stage during which the structure of the material does not alter. Amplitude sweep results (Fig. 7) in our study show similar behaviour and provide further evidence that the structure of the material did not change during sample loading.

The frequency or shear strain-rate dependence of a material is characterised using *frequency sweep tests* (Fig. 3a), during which the oscillation frequency is varied between 0.01 to 100 s^{-1} while the shear strain and temperature are held constant (γ = 1%, T = 22.5 °C). In order to remain in the linear viscoelastic domain, shear strain in this test was kept below γ_c determined by amplitude sweep tests. The resulting values of G′ and G″ were used to calculate the complex shear modulus from Eqn. 3. The complex Young's modulus was calculated from Eqn. 5, assuming LRD is incompressible with a Poisson ratio ν = 0.5. This assumption is reasonable because LRD is similar to the natural clay mineral Hectorite, and for most saturated clays reported Poisson ratios are close to 0.5. Further, the Maxwell relaxation time of the material can be determined from the frequency where the G′ and G″ curves cross each other (Fig. 3a).

In order to identify the effects of temperature on LRD, *temperature sweep tests* were performed by applying a slow heating rate (2 °C per minute) to the sample from 20 to 50 °C. For each 2 °C step the measurement duration was 1.07 min, during which the shear strain and oscillation frequency were kept constant within the linear viscoelastic range to ensure reproducibility of the results.

3.2.2 Rotational tests

The shear strength of LRD samples was measured using *rotational shear strength tests*, in which samples were deformed by imposing a shear strain up to 500 % at constant strain rate and temperature (0.1 s^{-1} and 22.5 °C). Shear stress of the material was recorded as a function of strain. The maximum shear stress here defines the shear strength or peak strength of the material.

Finally, *transient creep and recovery* tests were performed to measure the creep and recovery responses during the deformation of the material. A constant shear stress (τ = 70 Pa) was imposed on the sample for a pre-set time period (1210 s), and the shear stress was then removed abruptly (τ = 0 Pa) and the recovery of shear strain in the material was recorded over time. The initial constant shear stress value was selected based on the results of the amplitude and frequency sweep tests to ensure that the applied shear stress was within the linear viscoelastic region of the material.

4. Results

4.1. Amplitude sweep tests

The dynamic moduli of LRD mixtures (curing time = 3 days) determined by oscillatory amplitude sweep tests are presented in Table 1 and Figure 7. All concentrations of LRD are in the linear viscoelastic domain with constant G′ and G″ for shear strain amplitudes γ < 10 %.

The critical shear strain, γ_c, under which the material is in the linear viscoelastic region decreases with increasing concentration (Table 1; Fig. 7 - dotted lines). This γ_c was considered as the point at which moduli values (G′ and G″) change by 1 % from their constant plateau values (van Otterloo and Cruden, 2016). The shear strain amplitude at which G′ and G″ change rapidly by 15 % between two adjacent measurements is considered to be the yield limit (γ_L= 10 %). At this point, the material transitions from an effectively elastic regime to an effectively plastic regime. As shear strain increases above γ_L, G′ decreases and G″ increases rapidly until elastic and viscous forces exactly balance at G′ = G″ (Di Giuseppe et al., 2009). This occurs at shear strains of 26 % and 46.9 % for 2 wt. % and 4 wt. % concentrations, respectively (Fig. 7).

4.2. Frequency sweep tests

The results of the frequency sweep tests are presented in Table 2 and the dependence of G′ and G″ on frequency in the viscoelastic regime is shown in Fig 8a. G′ is approximately constant for all LRD samples over the full range of frequencies tested and the corresponding value of G″ drops as frequency is increased. However, G′ dominates over G″ by more than one order of magnitude within this frequency range. Both the dynamic moduli (G′, G″) and the complex shear (G*) and Young's (E*) moduli calculated using Equations 3 and 5 increase with the concentration of LRD and the sample age (Table 2; Fig. 8b).

4.3. Temperature sweep tests

The effective viscosity, η, of LRD mixtures measured at a slow heating rate of 2 °C per minute at constant shear strain rates, $\dot{\gamma}$, varies by 4 orders of magnitude as $\dot{\gamma}$ is increased from 0.01 s^{-1} (Fig. 9a) to 50 s^{-1} (Fig. 9b). The effective viscosity is nearly independent of temperature between 20 °C and 50 °C for LRD concentrations up to 2.5 wt.% for $\dot{\gamma}$ = 0.01 s^{-1} (Fig. 9a) and up to 3 wt.% for $\dot{\gamma}$ = 50 s^{-1}. Above these concentrations, the effective viscosity decreases significantly with increasing temperature at both strain rates. This decrease is greatest during the first few initial temperature increments for higher LRD concentrations (> 3.5 wt. %).

4.4. Rotational strength tests

Results of the rotational strength tests are presented in Table 3 and Figure 10. The stress-strain curves show that there is a strength increase with longer curing times (compare Fig. 10a and b). All concentrations show a linear viscoelastic response up to shear strain values of 10 % (i.e. the yield strength or limit) followed by a phase of strain hardening until a peak strength, τ_m (Pa), is reached when γ > 15 - 20 % (Fig. 10c). The peak strength value in Fig. 10, increases with LRD concentration and age (Fig. 11), while the corresponding shear strain is roughly constant. A decrease in shear stress values at strains beyond the peak stress indicates

a phase of strain softening (Fig. 10c). Shear stresses eventually reach constant values at high shear strains, corresponding to plastic deformation. The shear strength, τ_m (Pa) of different LRD concentrations is characterised by an empirical linear relationship with the sample age given in Fig. 11b.

4.5. Creep and recovery test

Results of the creep and recovery test for 4 wt. % LRD are presented in Fig. 12. During stress loading (τ = 70 Pa) at t = 0 s, shear strain (γ_0) increases instantaneously up to 0.0303 %. Then it shows a time dependent increase in viscoelastic (γ_{VE}) and visco-plastic (γ_{VP}) shear strain up to 0.0702 % when the shear stress is removed instantaneously (t = 1150 s). When the shear stress is removed, the recovery stage is characterized by an instantaneous drop in shear strain from 0.0702 % to 0.0454 %, corresponding to the elastic recovery (γ_E = 0.0248 %) of the sample. This elastic recovery is different from the initial instantaneous strain (γ_0 = 0.0303 %). The (γ_0 - γ_E) discrepancy is therefore considered to record an instantaneous time independent perfectly plastic strain, γ_P (Perl et al., 1983). After this, the material undergoes a period of time dependent, recoverable viscoelastic strain (γ_{VE}). During this recovery period between t = 1150 and 3840 s the shear strain decays, reaching a permanent, time independent shear strain ($\gamma_{VP} + \gamma_P$) of 0.0242 %. Results from the creep and recovery tests for different LRD concentrations (Table 5) at constant curing time (3 days) show a drop of the initial instantaneous strain, γ_0 from 0.0303 to 0.0228 % as concentration decreases from 4 to 3 wt. %, respectively. Moreover, as concentration is lowered, the values of γ_E and γ_{VP} decrease and the time independent plastic strain (γ_P) increases from 0.0055 to 0.0074 %. Similar shear strain (γ_E, γ_{VE}, γ_{VP} and γ_P) values are obtained for each concentration during the creep and recovery phases (see Table 5).

The shear strain versus time curve from this test shows the creep and recovery phases of the material, which are subdivided into different regions, representing characteristic mechanical behaviours of the sample. The creep phase has three distinct regions: (I) an initial instantaneous and time independent, elastic and perfectly plastic increase in shear strain in response to the applied instantaneous stress; (II) a secondary time-dependent viscoelastic response that will eventually be recovered when the stress is removed; and (III) a tertiary non-recoverable visco-plastic deformation. The recovery phase mirrors the same regions: an elastic recovery of the material due to the removal of the applied stress; delayed time-dependant viscoelastic recovery and a final non-recoverable component of permanent visco-plastic and plastic deformation, attributed to the visco-plastic response of the material.

5. Discussion

We investigated the rheological properties of LRD in order to assess its suitability as a crustal analogue for use in analogue modelling experiments. Physical parameters such as concentration, temperature and ageing time have been considered to fully characterise its range of mechanical properties, discussed below.

5.1. Rheology of Laponite RD

According to the rheological results presented above, LRD shows complex mechanical behaviours that vary from linear viscoelastic, non-linear viscoelastic, visco-plastic to plastic. The tests demonstrate that at low strains, characterisation of the linear and non-linear viscoelastic response of a material is important for predicting its deformation behaviour. As observed from the oscillatory tests, all measured concentrations of LRD in the gel state are viscoelastic (Figs. 7, 8). However, the linear viscoelastic region occurs below a critical strain amplitude, γ_c, which decreases from ~ 3% to ~ 1 % as concentration is increased from 2 to 4 wt. % (Table 1). In this LVE domain, the elastic storage modulus (G′) of LRD dominates over the loss modulus (G″), a measure of viscous dissipation, by two orders of magnitude (Fig. 7).

Beyond the critical shear strain that limits the LVE domain, the elastic properties of LRD decrease and its viscous properties become more important. Non-linear viscoelastic behaviour starts at this point, resulting in permanent deformation of the material. These behaviours can be explained by a Maxwell viscoelastic model (Fig. 4d), with a linear elastic component (spring) in series with a viscous component (dashpot). In this model the spring accommodates low amounts of recoverable elastic strain, and above γ_c permanent strain is accumulated in the viscous dashpot.

From the frequency sweep tests (Fig. 8) it is clear that, within the LVE domain, G′ is almost independent of the measured frequency range, except at very low frequencies (< 0.8 s^{-1}). At frequencies below 0.8 s^{-1}, G′ starts to decrease and G″ continuously increases. The Maxwell relaxation time (t_m), defined as the inverse frequency (i.e., $1/\omega = t_m$) at the crossover points of G′ and G″, could not be determined within the tested frequency range because such a crossover is not reached. Around the lowest frequency we could achieve (~2×10^{-1} s^{-1}, i.e., t = 5 s), G′ and G″ are still approaching each other. This places an upper bound on the Maxwell relaxation time of t_m > 5 s, which is higher than that of pig skin gelatine (0.3 – 1.5 s; van Otterloo and Cruden, 2016).

The storage (G′) and loss modulus (G″) values of LRD determined here (G′ = 6.28×10^1 – 3.23×10^3 Pa and G″ = 29 – 295 Pa at $\omega = 10^{-1}$ s^{-1} – 10^2 s^{-1}) are very similar to measurements by Willenbacher (1996), Mourchid et al. (1998) and Morariu and Bercea (2011).

However, Willenbacher (1996) and Mourchid et al. (1998) used LRD samples with different ionic strengths by adding NaCl, and Morariu and Bercea (2011) tested aqueous solutions of polyethylene glycol (PEG) containing LRD.

5.2. Comparison of the rheological properties of Laponite RD and gelatine

The G′ and G″ values of pig skin gelatine measured by frequency sweep tests (van Otterloo and Cruden, 2016) with a smaller frequency range ($\omega = 1 - 500\ s^{-1}$) vary from 4.25×10^4 - 2.88×10^4 Pa (T = 5 – 20 °C, $\omega = 1 - 500\ s^{-1}$ and X = 1 - 10 wt.%) and 4.22 - 49.6 Pa respectively, which are similar to values for LRD. The storage and loss modulus values are also similar to those reported for pig skin gelatine by Di Giuseppe et al. (2009; G′ 1.76×10^1 - 2.15×10^3 Pa and G″ 0.3 – 23.4 Pa at T = 10 °C and X = 1- 4 wt. %) and Brizzi et al. (2016; G′ $4.64 \times 10^1 - 7.23 \times 10^2$ Pa and G″ 1.37 – 14.1 Pa at T = 10 °C and X = 2.5 wt. %). However, Brizzi et al. (2016) used pig skin gelatine (2.5 wt. %) with different concentrations of NaCl, finding that, for the same gelatine concentration, G′ and G″ values decrease as the NaCl concentration increases. The maximum shear strain (γ_c) at which LRD deforms in the linear viscoelastic domain is similar to pig skin gelatine. In LRD γ_c is higher (> 2.16 %) for concentrations < 3 wt. % and lower for concentrations > 3 wt. % (see Table 1). In pig skin gelatine, γ_c is higher (10 % - 21.5 %) for lower concentrations < 3 wt.% and lower (3.16 %) for concentrations > 5 wt.% (van Otterloo and Cruden, 2016). However, γ_c values for pig skin gelatine are higher than those of LRD at similar concentrations. Hence, for similar concentrations, the critical shear strain (γ_c) of LRD is lower than that of gelatine.

The calculated Young's modulus values of LRD (1.05×10^3 - 1.18×10^4 Pa at T = 22. 5 °C) are similar to those reported for gelatine by Kavanagh et al. (2013; 4.4×10^3 - 1.5×10^4 Pa at T = 5 °C and X < 4 wt. %) and Van Otterloo and Cruden (2016; 10^3 - 10^4 Pa at T = 5 °C and X < 5 wt. %). The complex shear modulus values of LRD (3.49×10^2 - 3.92×10^3 Pa at T = 22. 5 °C) are also similar to those reported for pig skin gelatine (Van Otterloo and Cruden, 2016; $6.34 \times 10^2 - 7.02 \times 10^3$ Pa at T = 5 °C and X = 3-10 wt. %).

The peak strength values of 4 wt.% LRD samples after 7 and 14 days of curation are 258 Pa and 385 Pa, respectively, similar to the those reported by Wallace and Rutherford (2015; 300 Pa and 360 Pa) who used a shear vane method to measure the peak undrained shear strength of LRD. The maximum shear strength values of gelatine (823 – 12,000 Pa at T = 5 °C, X = 1-4 wt. %) are one to two orders of magnitude higher than the LRD concentrations measured here (Van Otterloo and Cruden, 2016). Shear strain values corresponding to the peak strength of gelatine vary from 167 – 127 % as concentrations increase from 1 – 4 wt.% (Van Otterloo and

Cruden, 2016), while the maximum peak strength shear strain values of the LRD concentrations measured here vary between 15 and 20 %.

5.3. Implications for the use of Laponite RD as a rock analogue

Our results reveal that the stress-strain behaviour of all LRD concentrations changes from linear viscoelastic to plastic, after undergoing a sequence of yielding, strain hardening, peak strength and strain softening processes (Fig. 10), similar to the low temperature stress-strain behaviour of natural rocks under confining pressure (Giuseppe et al., 2009). At shear strain rates of 0.01 s^{-1} and shear strain amplitudes $\gamma < 10$ %, all LRD concentrations behave predominantly elastically and can therefore be used to model brittle elastic deformation of rocks with different mechanical properties (e.g., Young's modulus). These properties will depend on the concentration of LRD and the curing time (Equations 6 -10). At shear strain rates of 0.1 s^{-1} and strain amplitudes $\gamma > 26.2$ %, LRD can be used to model plastic deformation of rocks (Fig. 10c).

Figure 13 presents a rheological model for 2 – 4 wt. % concentrations of LRD based on the various test results reported here. LRD is best described as combining a Bingham-Maxwell (elasto-visco-plastic) model and a Kelvin-Voight (viscoelastic) model in series with an additional frictional element. This behaviour is linked to the creep and recovery test results in Fig. 12. During the initial stress loading, the instantaneous and time independent elastic (γ_E) and plastic strains (γ_P) in region I are represented by the E_1 spring and the frictional element (F). The recoverable and time dependant viscoelastic (γ_{VE}; region II) behaviour is modelled by the Kelvin-Voigt viscoelastic element (E_2, η_2). The non-recoverable and time dependant visco-plastic (γ_{VP}; region III) response of LRD during the steady state creep phase is described by dashpot (η_1) and plastic (F) elements are in parallel. This creep and recovery behaviour is similar to a Burgers model (see Fig. 4h). However, a Burgers model only accounts for the instantaneous elastic strain component, not the instantaneous plastic strain component observed in our creep and recovery tests (Fig. 12).

5.4. Application to magma intrusion experiments

Different types of gels are commonly used as crack formation and propagation media to model sill and dyke emplacement in laboratory experiments (Kavanagh et al., 2006; Bertelsen et al., 2018b). Here we present two examples of how different concentrations of LRD may be used as crustal analogues for magma intrusion experiments. The experimental set up (Fig. 14a) is designed to facilitate lateral emplacement of sills at different crustal levels. Two layers (L_1 - bottom, L_2 - top) of LRD with the same concentration were placed into an open-topped plexiglass tank (30 cm x 30 cm x 6 cm) approximately one hour after each other. The

top layer solution was slowly poured through a tube along the walls of the tank to avoid any impact on the interface. Both the bottom and top layers at the time of pouring were at room temperature (22.5 °C). Therefore, temperature differences between the layers will have a negligible influence on the interface strength. This is further supported by temperature sweep test results (Fig. 9a,b), where the effective viscosity of LRD is either independent or varies only slightly (LRD 4wt. %) within a temperature range of 20 – 50 °C. Room temperature paraffin oil BP (Newtonian viscous; density = 0.85 g/cm^3) was then injected horizontally into the interface between the LRD layers via a nozzle at the side of the tank, fed by a peristaltic pump at a controlled flow rate (1 ml/min).

5.4.1. Scaling of magma intrusion experiments

We scaled our experiments to nature (Table 4) using the methods developed by Hubbert (1937) and Ramberg (1982), and used by Merle and Borgia (1996), Mathieu et al. (2008) and Galland et al. (2009). The principle is to define scaling factors and dimensionless numbers for the model, which simulates similar geometric, kinematic and dynamic processes in nature.

We have defined the length scaling factor (L*) as the ratio of the final length of a sill in the experiment (l_m) to the length of a sill in the shallow crust (l_n). In our case $L^* = l_m/l_p = 10^{-4}$ (1 cm represents 100 m). The density scaling factor $\rho^* = 0.357$ is the ratio between the density of LRD in the experiments and natural sedimentary host rocks, and the gravitational acceleration scaling factor $g^* = 1$. This gives a stress scaling factor

$$\sigma^* = \rho^* \cdot g^* \cdot L^* = 3.57 \times 10^{-5} \quad (5).$$

Natural magma intrusion velocities range from 0.1 m s^{-1} to 0.5 m s^{-1} (Spence and Turcotte, 1985; Kavanagh et al., 2013). Taking a lower intrusion velocity of 0.2 m s^{-1} and the average model intrusion velocity in our experiments of ~$1 \cdot 10^{-3}$ m s^{-1} gives a velocity scaling factor, $V^* = 5 \times 10^{-3}$. We can now define the time scaling factor as

$$t^* = L^*/V^* = 2 \times 10^{-2} \quad (6).$$

Using σ^* and t^*, the viscosity scaling factor is

$$\mu^* = t^*\sigma^* = 7.14 \cdot 10^{-7} \quad (7).$$

To scale the volumetric flow rate of the intruding magma we consider the density difference ($\Delta\rho^*$) and Young's modulus (E^*) ratios. Firstly, $\Delta\rho^* \sim 1.5$ is calculated using the ratio of the density differences between the host rock and the magma in the model and nature (Table 1). The Young's modulus measured for LRD concentrations used in the experiment after 7 days curing time is in the range 10^3 - 10^4 Pa. Young's moduli for upper crustal rocks ranges from 10^9 to 10^{10} Pa (Kavanagh et al., 2013), so E^* in our study is in the range 10^{-7} – 10^{-5} Pa.

Using $\Delta\rho^*$, L^*, $V^*$and E^* we can define the volumetric flow rate ratio:

$$Q^* = \Delta\rho^* L^{*3} E^{*-1} V^* = 6.25 \times 10^{-10} - 3.75 \times 10^{-7} \quad (8).$$

Therefore, our experiments represent host rocks that are ~$10^5 – 10^7$ times weaker than nature, and 1 min in our models represents 0.83 hrs in nature. The intruding liquid in the experiments corresponds to a magma with a viscosity of 10^4 Pas, which represents a basalt or basaltic andesite with low crystal content. The volumetric flow rate scaling factor gives values from 0.05 to 26.56 m^3s^{-1} in nature, which is in the range of natural values recorded for volcanic systems (Traversa et al., 2010; Chanceaux and Menand, 2016).

5.4.2. Experimental observations

In experiment A (L_1 = 2 wt.%, L_2 = 2 wt.% LRD), the injected paraffin oil formed a perfect sphere or blob (Figs. 14b, c) at the needle tip, which then expanded upward through L_1 by increasing its diameter. From Figures 8b and 10 it is clear that the Young's modulus and yield stress of 2wt. % LRD are low. Therefore, 2 wt. % LRD is capable of undergoing visco-plastic flow after yielding and its behaviour is almost fluid-like. Due to this visco-plastic flow behaviour under low stresses, the elastic strain energy of the growing intrusion is dissipated before a crack can form. Since there was no evidence for brittle failure in this experiment, we interpret the paraffin oil intrusion to have been emplaced by visco-plastic yielding of the LRD and ballooning.

In experiment B, with higher concentration LRD (L_1 = 3 wt. %, L_2 = 3 wt. %) the paraffin oil was emplaced by brittle sill propagation. An initial flat inner sill formed at the L_1/L_2 interface, followed by the formation of an inclined sheet (after 190 s) to define a saucer-shaped intrusion (Figs. 14d, e). Finger-like geometries and offset lobate segments (Figs. 14d,e; blue lines) formed during sill propagation, resembling features observed at the margins of sill complexes in nature (Thomson and Hutton, 2004; Magee et al., 2016a). The horizontal inner sill (at the interface) and the inclined outer saucer segments indicate brittle, tensile fracture propagation mechanisms. Therefore, under the experimental conditions reported here, higher concentrations of LRD behave like solids and form tensile brittle cracks, which are favoured over spherical intrusions to minimise elastic strain energy. This is because the elastic strain energy of a penny-shaped crack is significantly less than that of a sphere (Kato et al., 1996). The formation of finger-like geometries and lobe segments may be related to the development of elasto-viscoplastic instabilities at the propagating sill front (e.g., Eslami and Taghavi, 2017; Pihler-Puzović et al., 2018). However, further discussion of such instabilities is beyond the scope of the present paper and is the subject of future work in preparation.

The 3D intrusion experiments presented here show different structural and geometrical behaviours to the experiments reported by Bertelsen et al. (2018), in which oil was injected vertically into Laponite bounded by two vertical, parallel glass plates spaced 5 mm apart (i.e., a Hele-Shaw cell). At high concentrations (3.5 wt. %) and very low curing times (~0 min), the oil intrusions have round shapes, which Bertelsen et al. (2018) attributed to viscous flow of the LRD. In our experiments, lower LRD concentrations (2 wt. %) and longer curing times (3 days result in 3D blob-like intrusions (Fig. 14. b, c), which we argue were controlled by plastic yielding and flow of the gel. At such low concentrations in our experiments, the intrusion shape is not influenced by the relatively weak interface between the two layers (Kavanagh et al., 2015), suggesting that the gel structure of LRD may not be fully formed, but still behave like weak solid with very low Young's Modulus and complex shear modulus values (Fig. 8). This is further supported by rotational strength tests of 2 and 2.5 wt. % LRD, which determined very low yield stress and peak strength values, and almost ideally plastic post-yielding behaviour (Fig. 10).

For longer curing times (40 – 240 min) and higher LRD concentration (3 wt. %), oil intrusions in Bertelsen et al.'s (2019) experiments propagated either by viscoelastic fracturing, shear faulting or elastic tensile fracturing, or a combination of all three. At higher concentrations (Experiment B; 3 wt. %) and longer curing times, our experiment displayed a complex intrusion behaviour, forming a sill with finger-like segments at the propagating front, which eventually developed into a saucer-shape intrusion (Figs. 14d, e). In this case, the propagation of the intrusion was directly controlled by the interface between the layers. We infer from these observations that the LRD gel responded to the injection of oil by brittle elastic fracturing.

The combination of rheological measurements and preliminary experimental results presented here indicate that LRD is an ideal analogue material for modelling magma intrusions and fracture propagation in shallow crustal rocks. There is also considerable potential for the use of LRD in other analogue modelling applications such as fault development within landslides, studies of localized versus distributed faulting within the upper crust, as well as earthquake and subduction simulations. Because its mechanical properties vary significantly with concentration and curing time, displaying elastic, visco-elasto-plastic to plastic rheological behaviours depending on the applied strain and strain rates.

6. Conclusions

LRD is well suited as a brittle-elastic rock analogue for modelling upper crustal rocks during magma emplacement and fracture propagation. It has low surface tension, which minimizes surface tension effects in geological experiments and is chemically and biologically stable, which is advantageous for safe laboratory work. LRD is also fully transparent and photo-elastic so it can be used to visualise stress patterns in host-rock analogues (e.g., Bertelsen et al. 2018).

The rheological tests reported here characterise the mechanical behaviour of different concentrations of gel-forming LRD. Our results show that LRD is linear viscoelastic with elasticity dominated mechanical properties at low shear strains (<10 %, shear rate = 0.1 s^{-1}). At higher shear strains (>26.2 %) all LRD concentrations show permanent plastic deformation as shear strain increases. The transitions between these behaviours depend on the applied strain and strain rate, composition and curing time of the sample, and are much less effected by temperature.

LRD with concentrations from 2.5 wt. % to 4 wt. % are suitable analogues to model brittle elastic and plastic deformation of rocks in the Earth's crust. Concentrations above 4 wt. % are not recommended as they form a gel structure too quickly, which prevents proper mixing, resulting in clumps and trapping of air bubbles. To model brittle viscoelastic behaviour in the laboratory, shear strain amplitudes γ must be < 10% (at shear strain rate 0.1 s^{-1}). Plastic deformation occurs at shear strain amplitudes γ > 26.2 % and a more complex behaviour develops in between these strain limits. Hence, LRD has significant potential as a laboratory analogue modelling material because it reproduces the full range of upper crustal rock behaviours from elastic, visco-elasto-plastic to plastic.

Acknowledgements

We gratefully acknowledge financial support from the Australian Research Council Discovery Grant (DP 190102422) to A.R.C. A PhD scholarship (DIPRS) from Monash University (Melbourne) to U.S.N.A is greatly appreciated. We greatly thank Dr. Anja Slim (Monash University) for very useful discussions about material rheology.

References

Bailey, R.C., 2006. Large time step numerical modelling of the flow of Maxwell materials. Geophysical Journal International 164, 460–466. https://doi.org/10.1111/j.1365-246X.2005.02788.x

Barnes, S.J., Cruden, A.R., Arndt, N., Saumur, B.M., 2016. The mineral system approach applied to magmatic Ni – Cu – PGE sulphide deposits ☆. Ore Geology Reviews 76, 296–316. https://doi.org/10.1016/j.oregeorev.2015.06.012

Bertelsen, H.S., Rogers, B.D., Galland, O., Dumazer, G., Abbana Benanni, A., 2018a. Laboratory Modeling of Coeval Brittle and Ductile Deformation During Magma Emplacement Into Viscoelastic Rocks. Frontiers in Earth Science 6. https://doi.org/10.3389/feart.2018.00199

Bertelsen, H.S., Rogers, B.D., Galland, O., Dumazer, G., Benanni, A.A., 2018b. Laboratory modeling of coeval brittle and ductile deformation during magma emplacement into viscoelastic rocks. Frontiers in Earth Science 6, 5473. https://doi.org/10.3389/feart.2018.00199

Bonn, D., Kellay, H., Tanaka, H., Wegdam, G., Meunier, J., 1999. Laponite:What Is the Difference between a Gel and a Glass? Langmuir 15, 7534–7536. https://doi.org/10.1021/la990167t

Brizzi, S., Funiciello, F., Corbi, F., Di Giuseppe, E., Mojoli, G., 2016. Brizzi et al. (2016)_Salt matters_ How salt affects the rheological and physical properties of gelatine for analogue modelling _ Elsevier Enhanced Reader.pdf. https://doi.org/10.1016/j.tecto.2016.04.021

Bunger, A.P., Cruden, A.R., 2011. Modeling the growth of laccoliths and large mafic sills : Role of magma body forces. 116, 1–18. https://doi.org/10.1029/2010JB007648

Chanceaux, L., Menand, T., 2016. The effects of solidification on sill propagation dynamics and morphology. Earth and Planetary Science Letters 442, 39–50. https://doi.org/10.1016/j.epsl.2016.02.044

Chhabra, R.P., 2010. Non-Newtonian fluids: An introduction. Rheology of Complex Fluids 3–34. https://doi.org/10.1007/978-1-4419-6494-6_1

Cummins, H.Z., 2007. Liquid, glass, gel: The phases of colloidal Laponite. Journal of Non-

Crystalline Solids 353, 3891–3905. https://doi.org/10.1016/j.jnoncrysol.2007.02.066

Di Giuseppe, E., Funiciello, F., Corbi, F., Ranalli, G., Mojoli, G., 2009. Gelatins as rock analogs: A systematic study of their rheological and physical properties. Tectonophysics 473, 391–403. https://doi.org/10.1016/j.tecto.2009.03.012

Eslami, A., Taghavi, S.M., 2017. Viscous fingering regimes in elasto-visco-plastic fluids. Journal of Non-Newtonian Fluid Mechanics 243, 79–94. https://doi.org/10.1016/j.jnnfm.2017.03.007

Galland, O., Holohan, E., Vries, B.V.W. De, Burchardt, S., 2015. Laboratory Modelling of Volcano Plumbing Systems : A Review. https://doi.org/10.1007/11157

Galland, O., Planke, S., Neumann, E.R., Malthe-Sørenssen, A., 2009. Experimental modelling of shallow magma emplacement: Application to saucer-shaped intrusions. Earth and Planetary Science Letters 277, 373–383. https://doi.org/10.1016/j.epsl.2008.11.003

Galland, O., Secondary, C.A., Author, C., Galland, O., Holohan, E., Burchardt, S., Galland, O., n.d. Advances in Volcanology Laboratory Modelling of Volcano Plumbing Systems Chapter # Laboratory Modelling of Volcano Plumbing Systems Olivier Galland , Eoghan Holohan , Benjamin van Wyk de Vries , Steffi Burchardt.

Giuseppe, E. Di, Funiciello, F., Corbi, F., Ranalli, G., Mojoli, G., 2009. Tectonophysics Gelatins as rock analogs : A systematic study of their rheological and physical properties. Tectonophysics 473, 391–403. https://doi.org/10.1016/j.tecto.2009.03.012

Kato, M., Fujii, T., Onaka, S., 1996. Elastic strain energies of sphere, plate and needle inclusions. Materials Science and Engineering A 211, 95–103. https://doi.org/10.1016/0921-5093(95)10091-1

Kaushal, M., Joshi, Y.M., 2014. Linear viscoelasticity of soft glassy materials. Soft Matter 10, 1891–1894. https://doi.org/10.1039/c3sm52978a

Kavanagh, J.L., Boutelier, D., Cruden, A.R., 2015. The mechanics of sill inception, propagation and growth: Experimental evidence for rapid reduction in magmatic overpressure. Earth and Planetary Science Letters 421, 117–128. https://doi.org/10.1016/j.epsl.2015.03.038

Kavanagh, J.L., Engwell, S.L., Martin, S.A., 2018. A review of laboratory and numerical

modelling in volcanology. Solid Earth 9, 531–571.

Kavanagh, J.L., Menand, T., Daniels, K.A., 2013. Gelatine as a crustal analogue: Determining elastic properties for modelling magmatic intrusions. Tectonophysics 582, 101–111. https://doi.org/10.1016/j.tecto.2012.09.032

Kavanagh, J.L., Menand, T., Sparks, R.S.J., 2006. An experimental investigation of sill formation and propagation in layered elastic media. Earth and Planetary Science Letters 245, 799–813. https://doi.org/10.1016/j.epsl.2006.03.025

Lapasin, R., Abrami, M., Grassi, M., Šebenik, U., 2017. Rheology of Laponite-scleroglucan hydrogels. Carbohydrate Polymers 168, 290–300. https://doi.org/10.1016/j.carbpol.2017.03.068

Magee, C., Muirhead, J., Schofield, N., Walker, R.J., Galland, O., Holford, S., Spacapan, J., Jackson, C.A., Mccarthy, W., 2018. Structural signatures of igneous sheet intrusion propagation Craig. Journal of Structural Geology. https://doi.org/10.1016/j.jsg.2018.07.010.This

Magee, C., Muirhead, J.D., Karvelas, A., Holford, S.P., Jackson, C.A.L., Bastow, I.D., Schofield, N., Stevenson, C.T.E., Mclean, C., Mccarthy, W., Shtukert, O., 2016a. Lateral magma flow in mafic sill complexes. Geosphere 12, 809–841. https://doi.org/10.1130/GES01256.1

Magee, C., Muirhead, J.D., Karvelas, A., Holford, S.P., Jackson, C.A.L., Bastow, I.D., Schofield, N., Stevenson, C.T.E., McLean, C., McCarthy, W., Shtukert, O., 2016b. Lateral magma flow in mafic sill complexes. Geosphere 12, 809–841. https://doi.org/10.1130/GES01256.1

Mohanty, R.P., Joshi, Y.M., 2016. Chemical stability phase diagram of aqueous Laponite dispersions. Applied Clay Science 119, 243–248. https://doi.org/10.1016/j.clay.2015.10.021

Morariu, S., Lămătic, I., Bercea, M., 2009. Rheological behaviour of smectite aqueous dispersions. Revue Roumaine de Chimie 54, 975–980.

Mourchid, A., Lécolier, E., Van Damme, H., Levitz, P., 1998. On Viscoelastic, Birefringent, and Swelling Properties of Laponite Clay Suspensions: Revisited Phase Diagram. Langmuir 14, 4718–4723. https://doi.org/10.1021/la980117p

Naldrett, A.J., 1999. World-class Ni-Cu-PGE deposits: Key factors in their genesis. Mineralium Deposita 34, 227–240. https://doi.org/10.1007/s001260050200

Norris, J., Giese, R.F., Costanzo, P.M., Vanoss, C.J., 1993. The Surface Energies of Cation Substituted Laponite. Clay Minerals 28, 1–11. https://doi.org/10.1180/claymin.1993.028.1.01

Pek-Ing, A., Yee-Kwong, L., 2015. Surface chemistry and rheology of Laponite dispersions - Zeta potential, yield stress, ageing, fractal dimension and pyrophosphate. Applied Clay Science 107, 36–45. https://doi.org/10.1016/j.clay.2015.01.033

Pihler-Puzović, D., Peng, G.G., Lister, J.R., Heil, M., Juel, A., 2018. Viscous fingering in a radial elastic-walled Hele-Shaw cell. Journal of Fluid Mechanics 849, 163–191. https://doi.org/10.1017/jfm.2018.404

Reber, J.E., Cooke, M.L., Dooley, T.P., 2020. What model material to use? A Review on rock analogs for structural geology and tectonics. Earth-Science Reviews 202. https://doi.org/10.1016/j.earscirev.2020.103107

Ruzicka, B., Zaccarelli, E., 2011. A fresh look at the Laponite phase diagram. Soft Matter 7, 1268–1286. https://doi.org/10.1039/c0sm00590h

Saumur, B.M., Cruden, A.R., 2016. On the emplacement of the voisey's bay intrusion (Labrador, Canada). Bulletin of the Geological Society of America 128, 147–168. https://doi.org/10.1130/B31240.1

Schmiedel, T., Galland, O., Haug, T., Dumazer, G., Breitkreuz, C., 2019. Coulomb failure of Earth's brittle crust controls growth, emplacement and shapes of igneous sills, saucer-shaped sills and laccoliths. Earth and Planetary Science Letters 510, 161–172. https://doi.org/10.1016/j.epsl.2019.01.011

Spence, D.A., Turcotte, D.L., 1985. Magma-driven propagation of cracks. Journal of Geophysical Research 90, 575–580.

ten Grotenhuis, S.M., Piazolo, S., Pakula, T., Passchier, C.W., Bons, P.D., 2002. Are polymers suitable rock analogs? Tectonophysics 350, 35–47. https://doi.org/10.1016/S0040-1951(02)00080-X

Thomson, K., Hutton, D., 2004. Geometry and growth of sill complexes: Insights using 3D seismic from the North Rockall Trough. Bulletin of Volcanology 66, 364–375.

https://doi.org/10.1007/s00445-003-0320-z

Traversa, P., Pinel, V., Grasso, J.R., 2010. A constant influx model for dike propagation: Implications for magma reservoir dynamics. Journal of Geophysical Research: Solid Earth 115, 1–18. https://doi.org/10.1029/2009JB006559

van Otterloo, J., Cruden, A.R., 2016. Rheology of pig skin gelatine: Defining the elastic domain and its thermal and mechanical properties for geological analogue experiment applications. Tectonophysics 683, 86–97. https://doi.org/10.1016/j.tecto.2016.06.019

Wallace, J.F., Rutherford, C.J., 2015. Geotechnical properties of LAPONITE RD®. Geotechnical Testing Journal 38, 574–587. https://doi.org/10.1520/GTJ20140211

Willenbacher, N., 1996. Unusual thixotropic properties of aqueous dispersions of Laponite RD. Journal of Colloid and Interface Science 182, 501–510. https://doi.org/10.1006/jcis.1996.0494

Xue, L., Qin, S.Q., Pan, X.H., Chen, H.R., Yang, B.C., 2017. A possible explanation of the stair-step brittle deformation evolutionary pattern of a rockslide. Geomatics, Natural Hazards and Risk 8, 1456–1476. https://doi.org/10.1080/19475705.2017.1345793

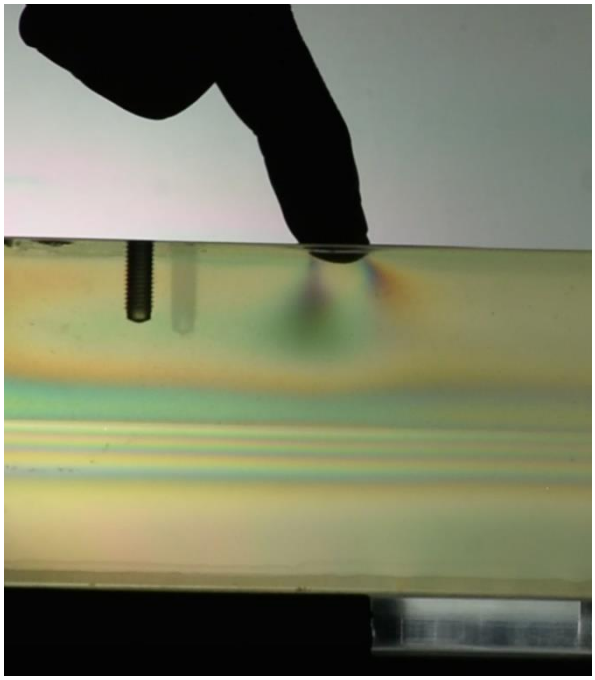

Fig. 1. (In colour in print) Photo-elastic fringes within a container of layered Laponite RD loaded from above, indicating the stress field induced by the applied force. Horizontal colour zones in the middle are due to photo-elastic effects caused by Laponite RD multi-layers.

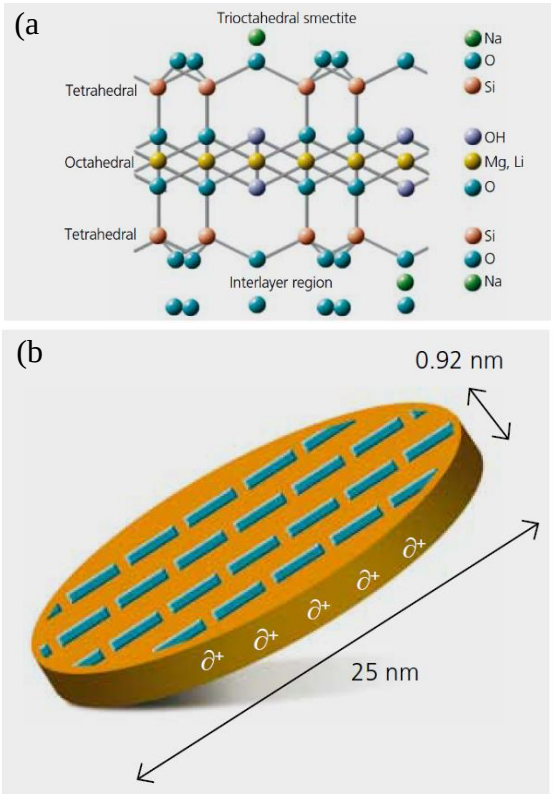

Fig. 2. (In colour in print) (a) Empirical formula and layered structure of individual Laponite particles. (b) Disc-shaped Laponite crystal with thickness (0.92 mm) and diameter (25 mm) with negatively charged faces and positively charged edges (BYK additives and instruments, 2014).

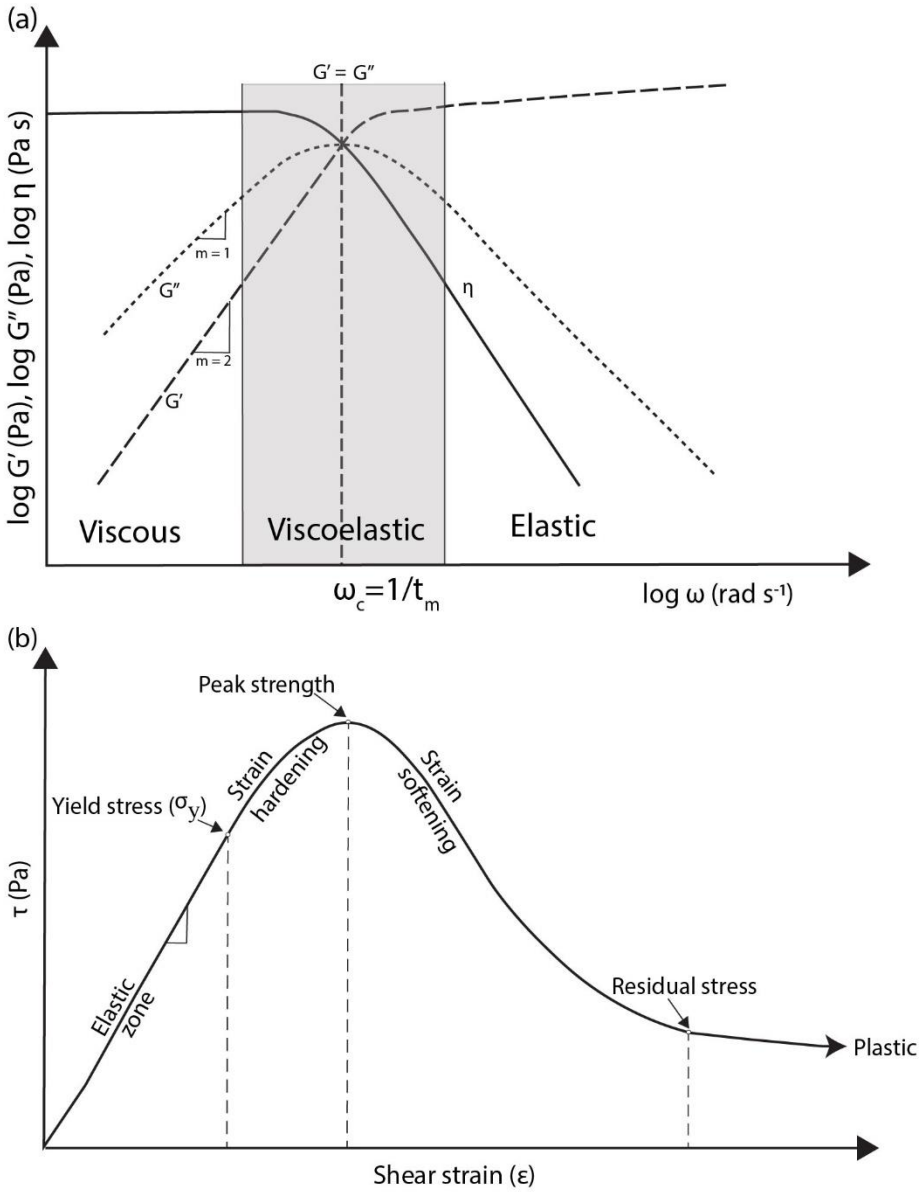

Fig. 3. (a) Typical rheological characterisation of an ideal linear viscoelastic material. Different fields indicate different mechanical behaviours, determined by the relation between storage (G′) and loss moduli (G″). At lower frequencies (ω), dominantly viscous behaviour is characterised by G″ >> G′ and the slopes of G″ and G′ are 1 and 2 respectively. In this viscous region, the complex viscosity (η*) is constant and similar to the zero-shear viscosity (η_0). At higher frequencies, dominantly elastic behaviour is characterised by G′ >> G″ and constant plateau of G′. Viscoelastic behaviour occurs at intermediate frequencies. The crossover point (ω_c) between G′ and G″ determines the Maxwell relaxation time (t_m) of the material (modified from Di Giuseppe et al., 2009). (b) Ideal shear stress – shear strain behaviour of strain softening rocks (modified from Xue et al., 2017) depicting a transition from elastic to plastic behaviour with post yielding strain hardening and strain softening behaviours (see text for details).

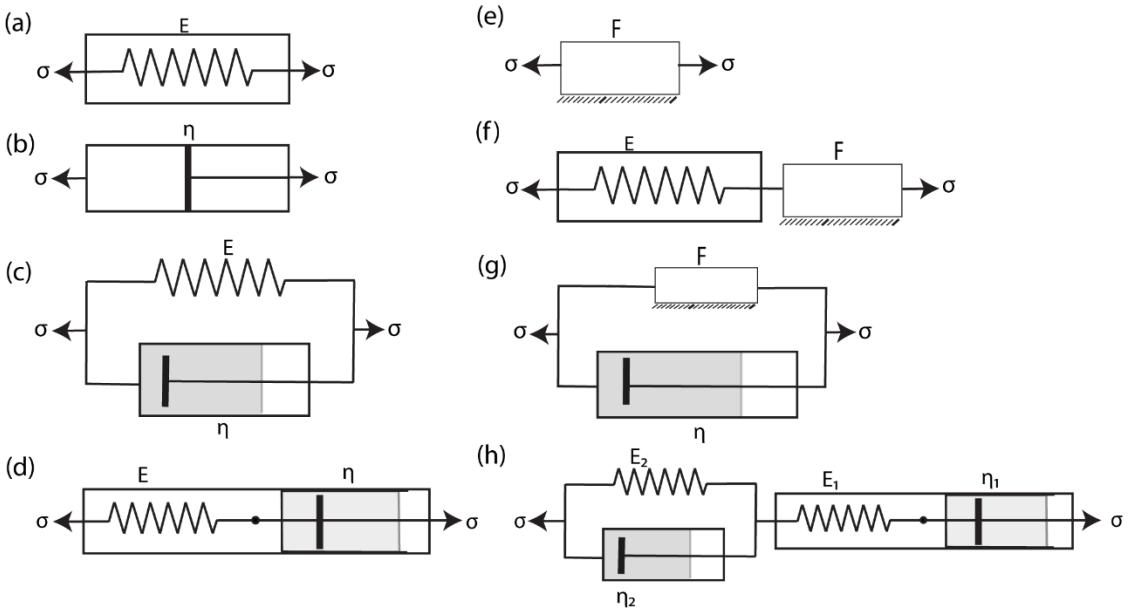

Fig. 4. Representation of basic rheological models. (a) Linear elastic (spring), (b) Linear viscous (dashpot), (c) Kelvin – Voight model (Visco-elastic), (d) Maxwell model (Visco-elastic), (e) Perfectly plastic (frictional element), (f) Linearly elastic- perfectly plastic model, (g) Bingham-Maxwell (Visco-plastic) model and (h) Burgers model.

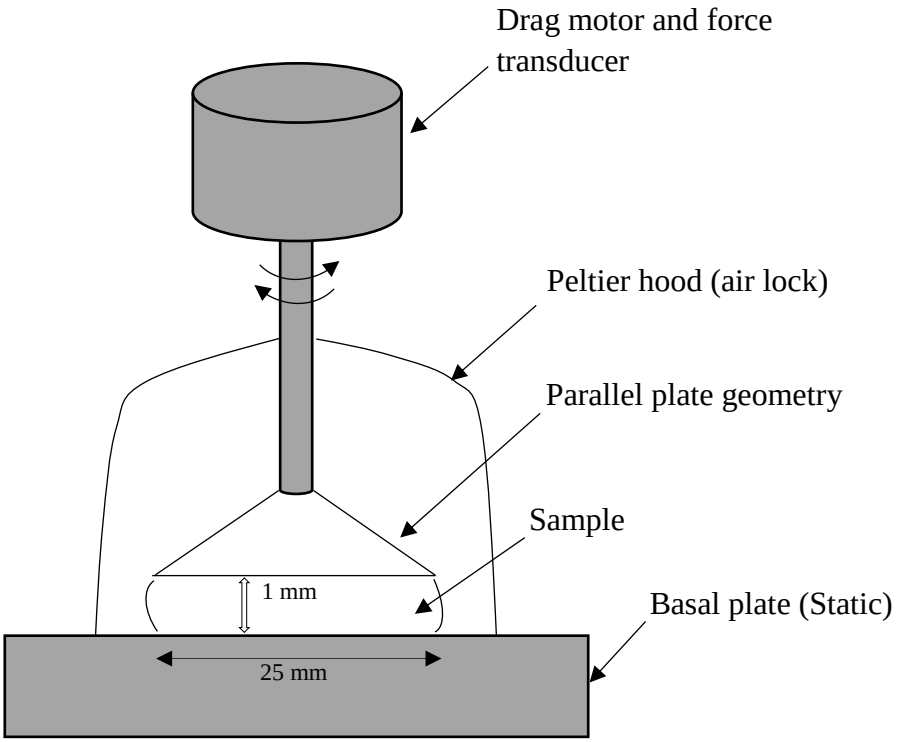

Fig. 5. Schematic diagram of a rheometer with a parallel-plate setup used for oscillation and rotational tests.

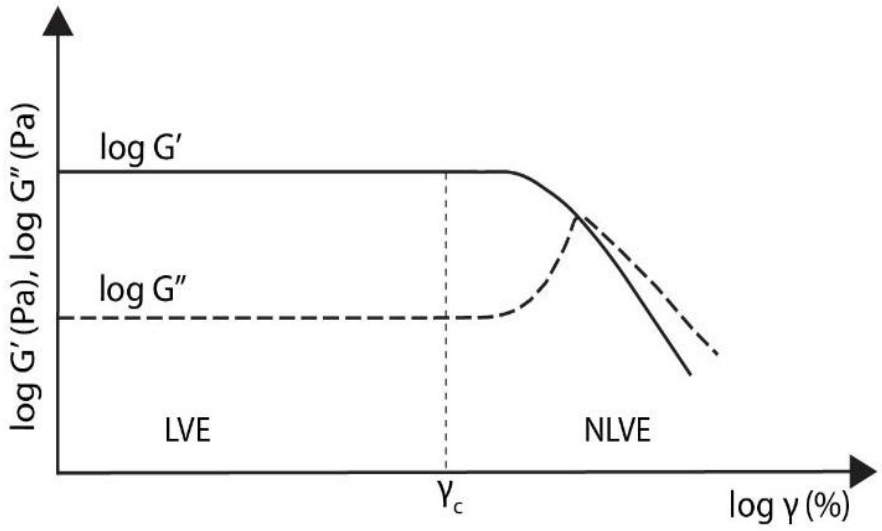

Fig. 6. Typical rheological behaviour of viscoelastic (VE) samples from oscillatory tests - here an amplitude sweep test for variable strain, γ (ω constant). Values of log G′ and log G″ show constant plateau values independent of strain amplitude (γ) in the linear viscoelastic (LVE) region, in which the structure of the sample is stable. Non-linear viscoelastic (NLVE) behaviour occurs above a critical shear strain (y_c). In this region the sample structure has been either irreversibly changed or destroyed.

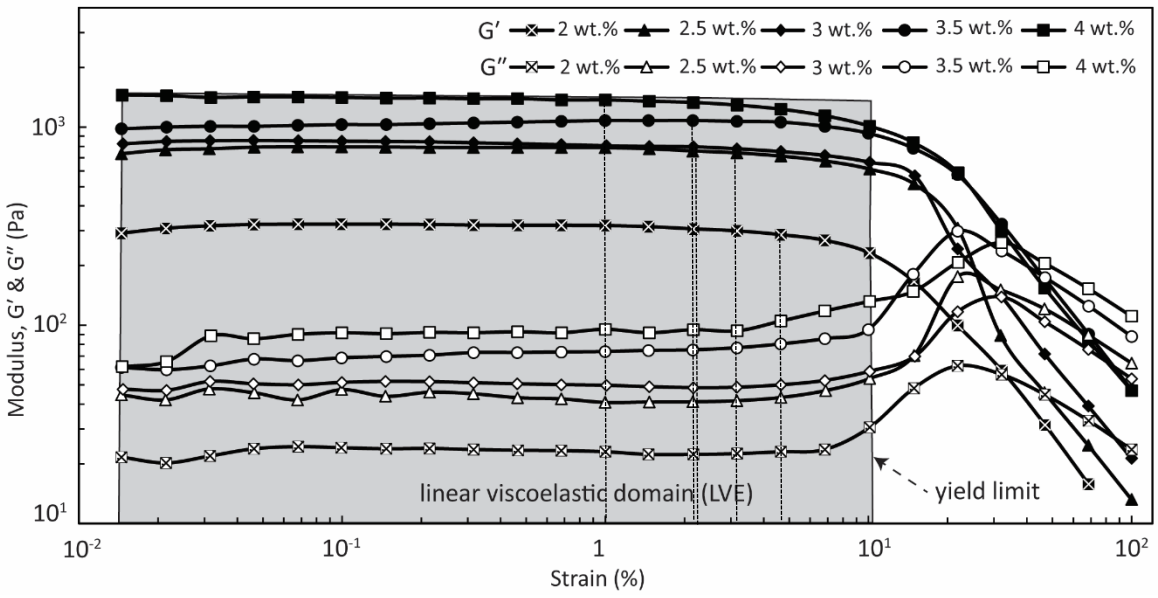

Fig. 7. Results from amplitude sweep tests showing variation of storage (G′) and loss (G″) moduli for Laponite RD with different wt. % concentrations and curing time of 3 days. Strain was varied from 0.01 % to 100 % at a constant strain rate (0.1 s^{-1}). The grey field (LVE domain) marks the values of the strain amplitude where the dynamic moduli, G′ and G″ remain nearly constant. The critical shear strains (γ_c) at which G′ and G″ start to change by 1 % from their constant plateau values are indicated by dotted lines for each concentration. The rapid change where G′ and G″ start to change by 15 % in between two adjacent measurements is considered here to define the yield limit.

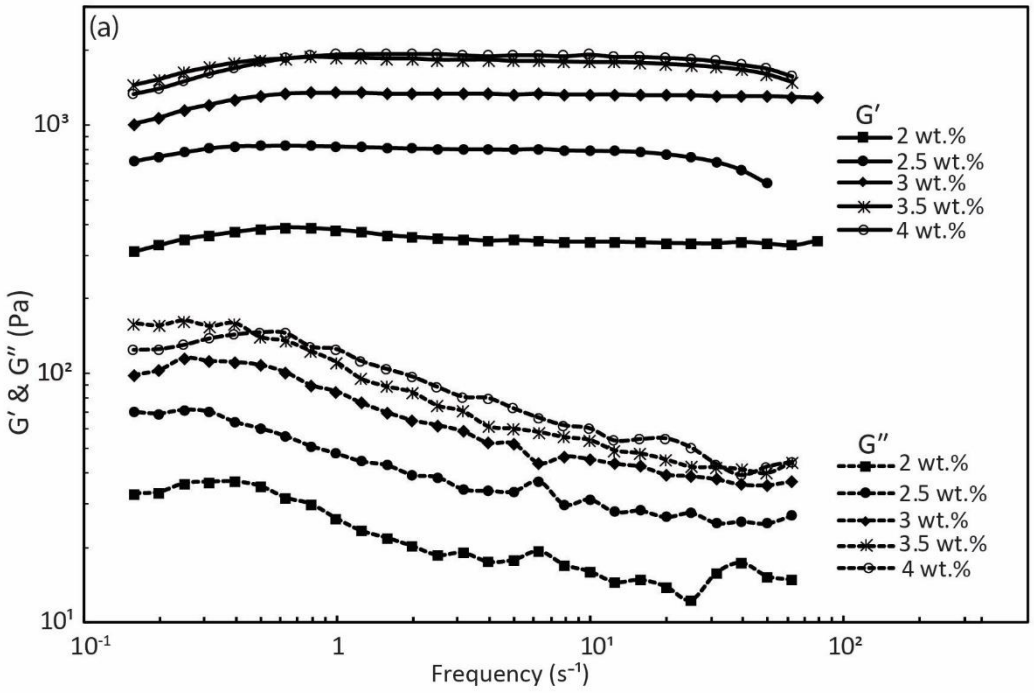

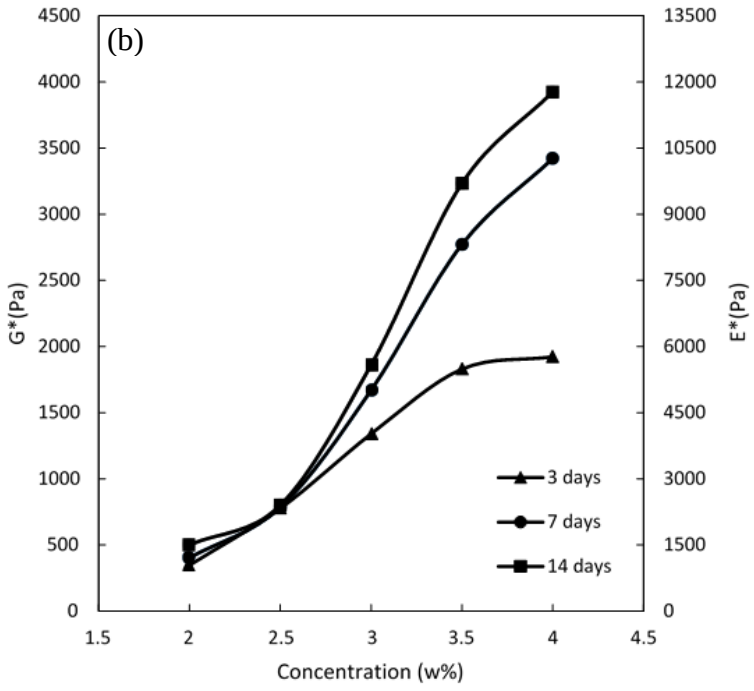

Fig. 8. Results from frequency sweep tests of Laponite RD showing the frequency dependence of dynamic moduli (a) Variations of storage, G′, and loss moduli , G″, values in the LVE domain ($\gamma < 1\%$) with change in frequency from 0.1 s^{-1} to 100 s^{-1}. (b) Calculated complex shear, G*, and Young's, E*, moduli values within the LVE domain for different Laponite RD concentrations and curing (aging) times.

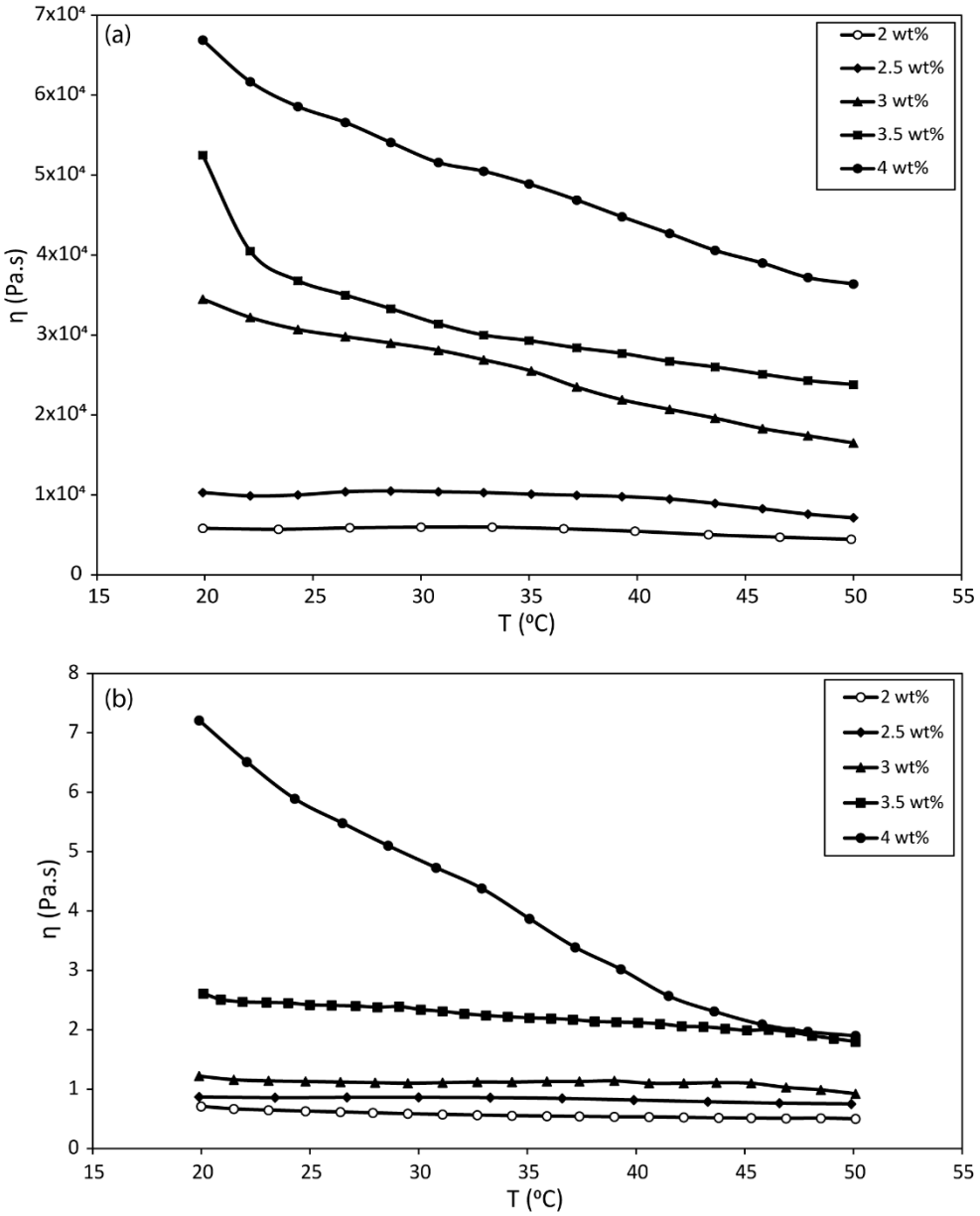

Fig. 9. Temperature dependence of viscosity for different concentrations of Laponite RD. Strain rate is constant at $0.01s^{-1}$ (a) and 50 s^{-1} (b). Note that the effective viscosity of LRD at low concentrations is not sensitive to temperature for both lower and higher strain rates. The effective viscosity does not vary at higher strain rate for all concentrations except 4 wt. %.

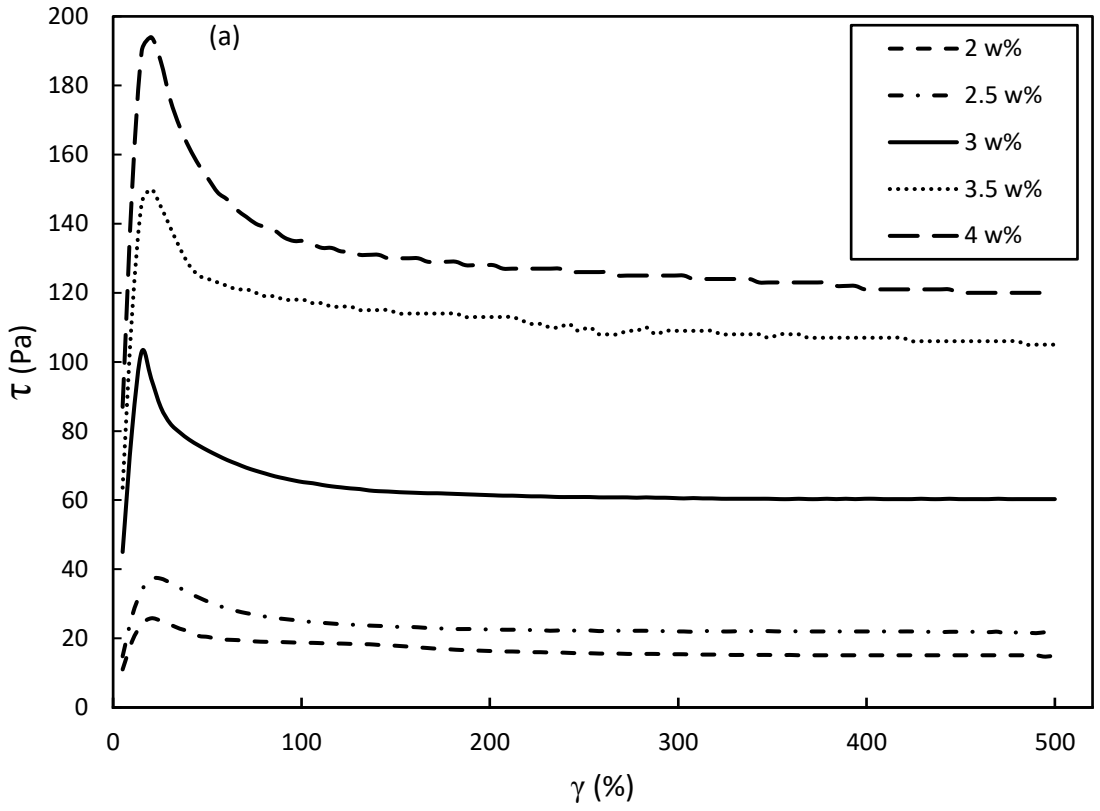

(Fig. 10: Figure caption on the following page)

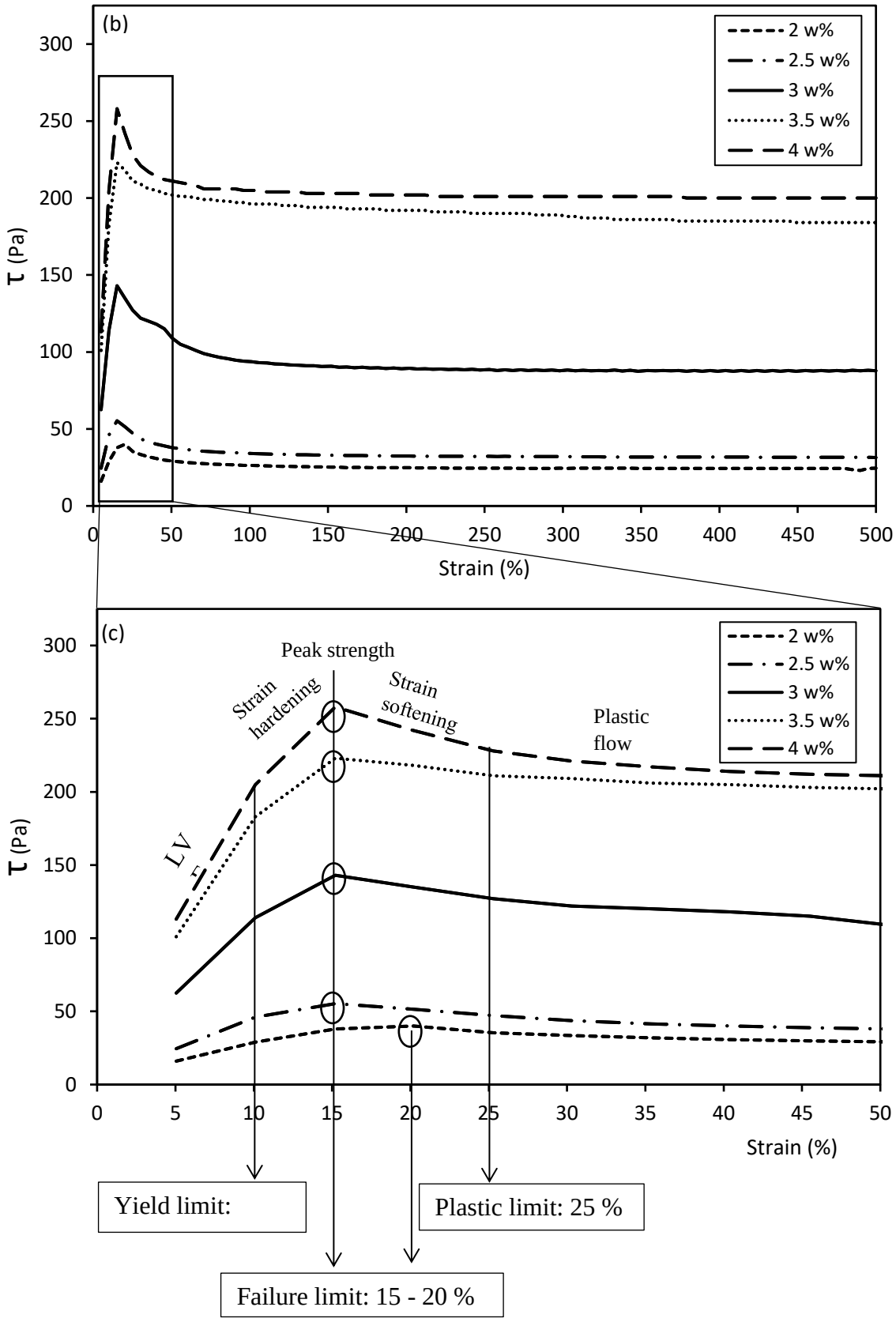

Fig. 10. Rotational strength test results for different Laponite RD concentrations showing shear stress variation for shear strains up to 500%. Strain rate is constant at 0.1 s^{-1}. The curing time varies from (a) 3 days to (b) 7 days. (c) Interpreted section of the lower shear strain region of (b).

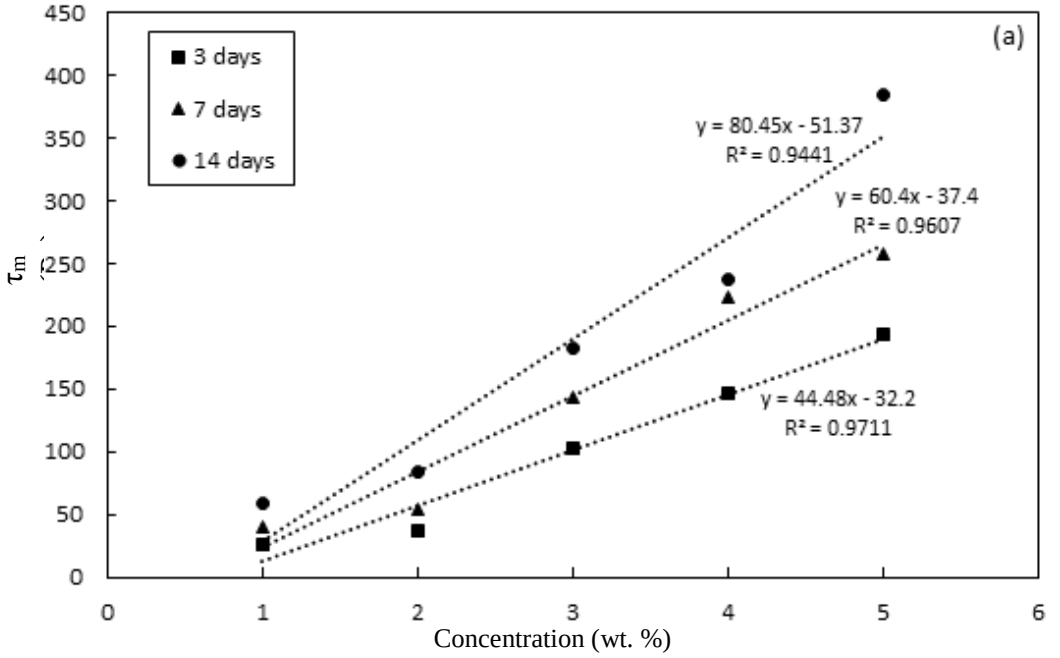

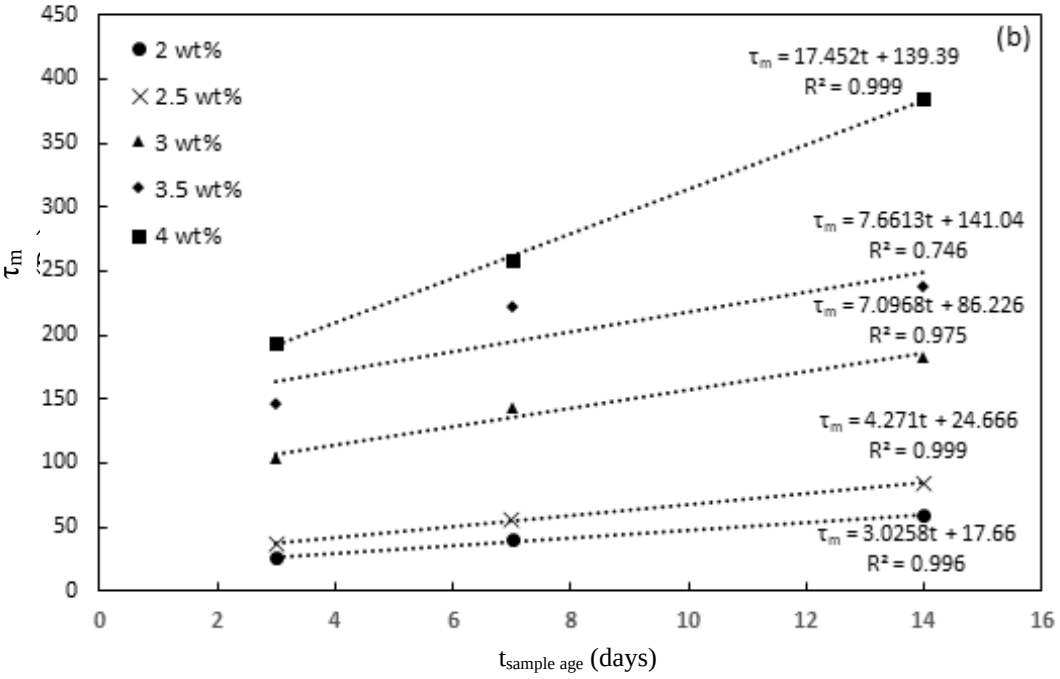

Fig. 11. (a) Maximum shear stress (i.e. shear strength, τ_m) versus Laponite RD concentrations for different curing times ($t_{sample\ age}$). (b) Shear strength versus curing time for each Laponite RD concentration.

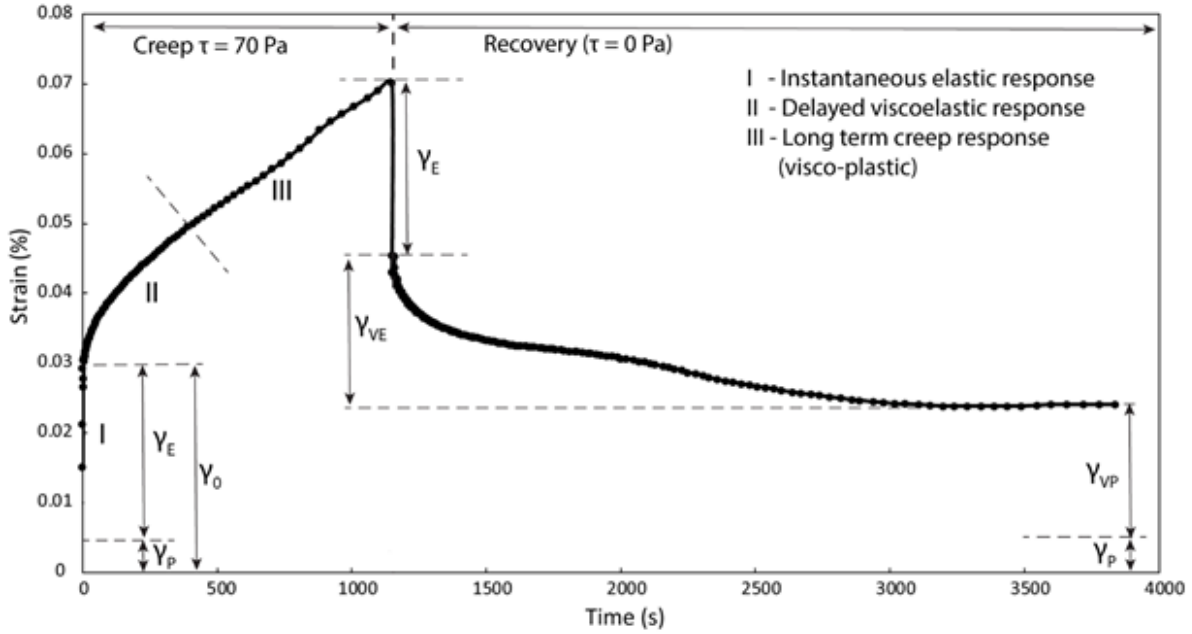

Fig. 12. Results of a creep and recovery test for 4 wt. % Laponite RD after 3 days of curing. Creep lasted t = 1150 s at a shear stresses τ = 70 Pa, after which the shear stress was set to 0 Pa and recovery started. Shear strains are marked as linear elastic (γ_E), perfectly plastic (γ_P), viscoelastic (γ_{VE}) and visco-plastic (γ_{VP}). γ_0 is the total instantaneous shear strain upon stress

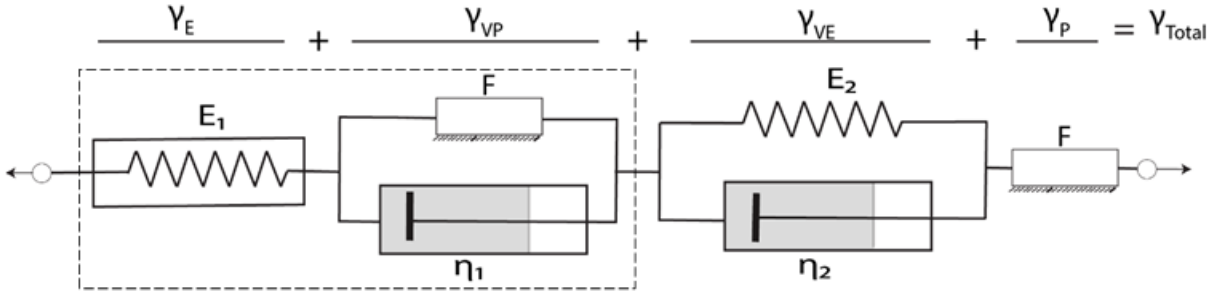

Fig. 13. Rheological model of Laponite RD based on creep and recovery tests (Fig. 12) and other rheological analyses. A Bingham - Maxwell model (E_1, η_1 and F; outlined in dotted line box) and Kelvin-Voigt (E_2, η_2) units are in series with an additional frictional element

5

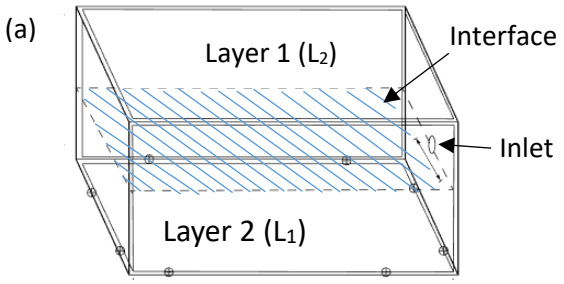

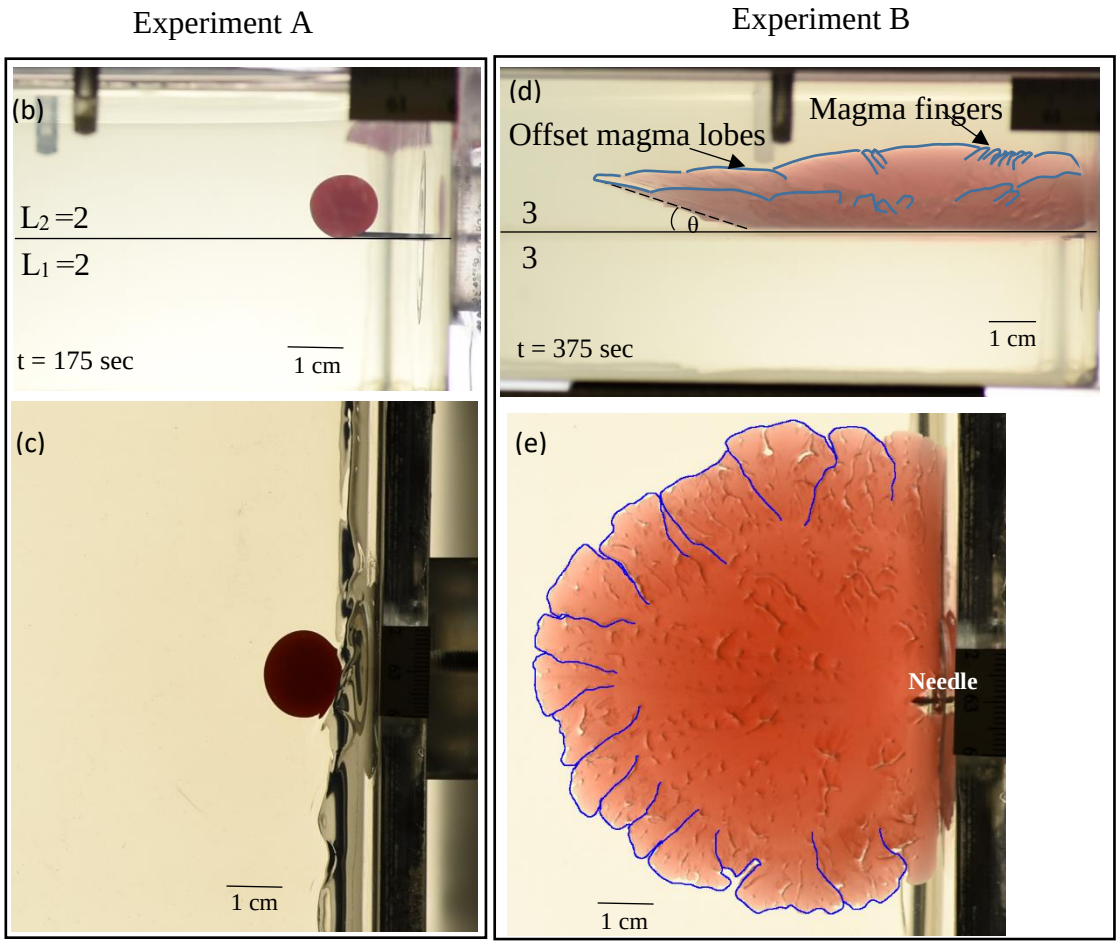

Fig. 14. (In colour in print) Magma intrusion experiments in which analogue magma (paraffin oil) is injected, via a needle and peristaltic pump, into LRD with different concentrations. Experimental set up (a) and results of experiment A (b, c) and B (d, e). Magma and host rock analogues are paraffin oil (red colour) and LRD (pale yellow colour) respectively. (b) side and (c) overhead view of experiment A with 2 wt.% LRD in both layers. (d) side and (e) overhead view of experiment B with 3 wt.% LRD layers. In experiment B (d, e), blue lines are traces of tip propagation geometries and θ (~25°) is the angle of the inclined sheet that formed at later stages. In (d) and (e) the intrusion formed a saucer-shaped sill, where the originally flat sill expanded along the L_1/L_2 interface until the tip changed orientation and propagated upwards forming a saucer-shape.

5 Tables

Table 1. Critical strain (γ_c) and corresponding G′ and G″ values for different concentrations (X wt. %) of Laponite RD (curing time – 3 days) from amplitude sweep tests.

X (wt.%)	γ_c (%)	G′ (Pa)	G″ (Pa)
2	4.65	286	23
2.5	3.16	740	41.60
3	2.16	796	48
3.5	2.15	1080	75
4	1	1370	95.40

Table 2. Results of frequency sweep tests applied to different concentrations and curing times of Laponite RD. The complex viscosity, η*, is the average value for the range of frequencies at which G′ and G″ were measured.

X (wt. %)	G′ (Pa)	G″ (Pa)	G* (Pa)	E* (Pa)	η* (Pa s)
3 days					
2	3.48×10^2	1.90×10^1	3.49×10^2	1.05×10^3	1.38×10^2
2.5	8.01×10^2	3.40×10^1	8.02×10^2	2.41×10^3	3.31×10^2
3	1.34×10^3	5.90×10^1	1.34×10^3	4.02×10^3	5.49×10^2
3.5	1.83×10^3	7.10×10^1	1.83×10^3	5.49×10^3	7.56×10^2
4	1.92×10^3	8.00×10^1	1.92×10^3	5.77×10^3	7.89×10^2
7 days					
2	4.05×10^2	2.00×10^1	4.05×10^2	1.22×10^3	1.64×10^2
2.5	7.77×10^2	3.58×10^1	7.78×10^2	2.33×10^3	3.20×10^2
3	1.67×10^3	6.60×10^1	1.67×10^3	5.01×10^3	6.88×10^2
3.5	2.77×10^3	1.16×10^2	2.77×10^3	8.32×10^3	1.86×10^2
4	3.84×10^3	1.73×10^2	3.42×10^3	1.03×10^4	1.88×10^2
14 days					
2	5.01×10^2	2.50×10^1	5.02×10^2	1.50×10^3	2.04×10^2
2.5	7.85×10^2	3.30×10^1	7.86×10^2	2.36×10^3	3.25×10^2
3	1.86×10^3	7.90×10^1	1.86×10^3	5.59×10^3	7.75×10^2
3.5	3.23×10^3	1.49×10^2	3.23×10^3	9.70×10^3	1.35×10^3
4	3.92×10^3	1.82×10^2	3.92×10^3	1.18×10^4	1.77×10^4

Table 3. Results of rotational strength tests and the corresponding maximum shear strength (τ_m) and shear strain (γ) for different sample ages and Laponite RD concentrations.

X	3 days		7 days		14 days	
(wt. %)	γ (%)	τ_m (Pa)	γ(%)	τ_m (Pa)	γ (%)	τ_m (Pa)
2	20.2	26	20.2	40	20.2	59
2.5	20.2	37.2	15.2	55	15.2	84
3	15.2	103	15.2	143	15.2	183
3.5	20.2	150	15.2	223	15.2	238
4	20.2	194	15.2	258	15.2	385

Table 4. Experimental variables and their corresponding values in nature.

Parameter	Dimension	Definition	Value		
			Nature (n)	Model (m)	Ratio*(m/n)
ρ_h	Kg m^{-3}	Host rock density	2800	1000	0.357
ρ_i	Kg m^{-3}	Intrusion (magma) density	2700	850	0.3
G	m s^{-2}	Gravity acceleration	9.81	9.81	1
V_i	m s^{-1}	Intrusion velocity	0.2	10^{-3}	$5x10^{-3}$
L	m	Length	100	0.01	10^{-4}
t	s	Time	-	900-2700	$2 \cdot 10^{-2}$
μ	Pa s	Magma viscosity	$2.2x10^{5}$	0.16	$7.14x10^{-7}$
Q_i	m^3 s^{-1}	Intrusion volumetric flow rate	(0.02 - 13.28)	$1.66x10^{-9}$	($6.25x10^{-10}$ - $3.75x10^{-7}$)

Scaling factors: model/nature	$\mathbf{L^* = 10^{-4}}$; $\mathbf{\rho^* = 0.357}$; $\mathbf{g^* = 1}$
Stress scaling factor	$\mathbf{\sigma^* = \rho^* g^* L = 3.57x10^{-5}}$ Model is 10^5 times weaker than in nature
Time scaling factor	$\mathbf{t^* = L^*/V^* = 2x10^{-2}}$ 1 min in model ~0.83 hr in nature
Viscosity scaling factor	$\mathbf{\mu^* = t^* \sigma^* \rightarrow \mu^* = 7.14x10^{-7}}$ Intrusion liquid represents magma with viscosity ~10^4 Pa s
Volumetric flow rate scaling factor	$\mathbf{Q^* = \Delta\rho^* L^{*3} E^{*-1} V^* = (6.25x10^{-10} - 3.75x10^{-7})}$ Experimental volumetric flow rate scales to 0.02 – 13.28 $m^3 s^{-1}$ in nature

Table 5. Shear strains under different mechanical regimes measured during creep and recovery phases for different LRD concentrations. Curing time is constant (3 days). See text for the definition of symbols.

LRD	Creep phase					Recovery phase			
(wt. %)	γ_0	γ_E	γ_{VE}	γ_{VP}	γ_P	γ_E	γ_{VE}	γ_{VP}	γ_P
4	0.0303	0.0248	0.0214	0.0187	0.0055	0.0248	0.0214	0.0187	0.0055
3.5	0.0261	0.0194	0.0239	0.0097	0.0067	0.0194	0.0239	0.0097	0.0194
3	0.0228	0.0154	0.0255	0.0067	0.0074	0.0154	0.0255	0.0067	0.0074